Polyhedron 165 (2019) 125–131

Contents lists available at ScienceDirect

Polyhedron

journal homepage: www.elsevier.com/locate/poly

Lanthanide mononuclear complexes with a tridentate Schiff base ligand: Structures, spectroscopies and properties

Yingjie Zhang [a,*], Maxim Avdeev [a], Jason R. Price [b], Inna Karatchevtseva [a], Daniel J. Fanna [c], Ilkay Chironi [a], Kim Lu [a]

[a] Australian Nuclear Science and Technology Organisation, Locked Bag 2001, Kirrawee DC, NSW 2232, Australia
[b] Australian Synchrotron, 800 Blackburn Road, Clayton, Victoria, Australia
[c] School of Science and Health, Western Sydney University, Locked Bag 1797, Penrith, NSW 2751, Australia

ARTICLE INFO

Article history:
Received 5 February 2019
Accepted 12 March 2019
Available online 21 March 2019

Keywords:
Lanthanide
Complex
Schiff base
Julolidine
Quinoline

ABSTRACT

A series of six lanthanide mononuclear complexes with a julolidine-quinoline based tridentate Schiff base ligand have been synthesized and structurally characterized. The complexes [Nd**L**$_2$(CH_3OH)(NO_3)]·CH_3OH (**1**) and [Ln**L**$_2$(NO_3)] [Ln = Eu (**2**), Gd (**3**), Dy (**4**), Ho (**5**), Lu (**6**)] {H**L** ($C_{22}H_{21}N_3O$) = ((E)-9-((quinolin-8-ylimino)methyl)-1,2,3,5,6,7-hexahydropyrido[3,2,1-ij]quinolin-8-ol)} all have mononuclear structures with a metal to ligand ratio of 1:2. The Ln(III) ions are nine-fold coordinated by two tridentate Schiff base ligands and a bidentate nitrate anion except for complex **1** in which Nd(III) ion is ten-fold coordinated with an additional MeOH molecule. The coordination of a bidentate nitrate anion makes chirality to the complexes with equal enantiomers presence in the solid state. Lanthanide contraction has been observed with the average Ln–O/Ln–N bond lengths decreasing along the lanthanide series. Vibrational modes (**2**–**5**), electronic structures (**1**–**3**), thermal stability (**2**) and magnetic properties (**3**) have been further investigated and reported.

1. Introduction

The julolidine function group is well known for its visible and fluorescent optical properties [1]. Consequently, it has become a popular base material for use in colorimetric metallo-supramolecular research. The versatility of julolidine has also been established with many chemosensor systems identified that exhibit targeted detection of specific molecular unit, often a metal ion [2] or an anion [3]. Due to the fluorescent nature of julolidine, fluorescence sensor systems have also been explored [4,5].

The Schiff base ligand adopted in the present study consists of 8-hydroxyjulolidine-9-carboxaldehyde and 8-aminoquinoline in a 1:1 synthesis [6], H**L** (see Fig. 1). Previous studies have demonstrated the potential of H**L** as a Co(II) chemosensor, and a complex of Co**L**$_2$ was confirmed by ESI-MS [6] and single crystal analysis [7]. Several types of transition metal complexes with H**L** have been reported including 1:1 and 1:2 monomeric structures for 3d metal ions [7] as well as complexes with dioxo-metal ions such as dioxo-vanadium, dioxo-rhenium and dioxo-uranium [8]. For lanthanide complexes with H**L**, two types of dimeric structures bridging with either acetate or methanol have been previously reported [9]. However, the current contribution deals with the formation of lanthanide mononuclear complexes with H**L**. Herein we report the syntheses, structures, spectroscopies and properties of six new lanthanide complexes: [Nd**L**$_2$(CH_3OH)(NO_3)]·CH_3OH (**1**) and [Ln**L**$_2$(NO_3)] [Ln = Eu (**2**), Gd (**3**), Dy (**4**), Ho (**5**), Lu (**6**)].

2. Results and discussion

2.1. Synthesis and general characterizations

Complexes **1**–**6** were prepared by direct reactions of Ln(III) nitrates and H**L** in methanol with added triethylamine for deprotonation. Scanning electron microscope-energy dispersive spectroscopy (SEM-EDS) was used to check the morphologies of the crystalline products and to probe the key elements present (Figs. S1–S2). Powder X-ray diffraction (PXRD) patterns of complexes **2** (Fig. S3a) and **3** (Fig. S3b) measured at room temperature are consistent with the patterns simulated from their single crystal data suggesting pure phase crystalline materials have been obtained.

* Corresponding author.
E-mail address: yzx@ansto.gov.au (Y. Zhang).

https://doi.org/10.1016/j.poly.2019.03.017
0277-5387/

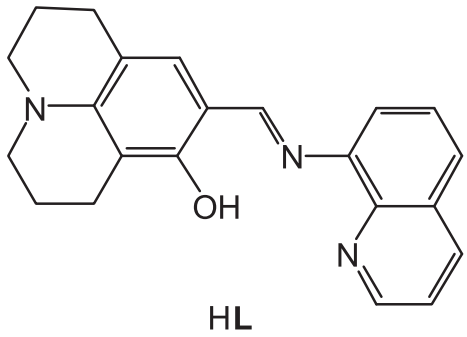

Fig. 1. A chemical structure of the Schiff base ligand H**L**.

2.2. Crystal structures and discussion

The crystal data and structure refinement details for complexes **1**–**6** are summarized in Table 1. Selected bond lengths for Ln(III) ions coordination environments are listed in Table 2. Complex **1** has a mononuclear structure (Fig. 2a) with a Nd(III) ion nine-fold coordinated by two tridentate deprotonated H**L** ligands [2.629 (3) Å for Nd1–N1, 2.603(3) Å for Nd1–N2 and 2.256(2) Å for Nd1–O1; 2.696(3) Å for Nd1–N4, 2.626(3) Å for Nd1–N5 and 2.319 (2) Å for Nd1–O2], a bidentate nitrate anion [2.607(3) Å for Nd1–O3 and 2.580(2) Å for Nd1–O4] and a monodentate methanol molecule [2.579(2) Å for Nd1–O6] making a distorted capped square antiprism for the Nd(III) ion coordination environment (Fig. S4). The two coordinated **L** ligands are twisted to form CH-π interactions (Fig. 2b) between each other. Such intramolecular CH-π interactions have not been observed in complexes of H**L** with either 3d transition metal ions [7] or dioxo-metal ions [8]. The Hydrogen bonds among lattice, coordinated methanol molecules and O2 atom link the mononuclear structures into a hydrogen bonded 1D polymer (Fig. 2c, Table 3). The coordination of the nitrate anion makes chirality of the complex with equal enantiomers presence in the crystal lattice (Fig. 2d). Intermolecular CH-π interactions are also present between mononuclear structures in the crystal lattice (Fig. 3a).

Complexes **2**–**6** have very similar mononuclear structures with the Ln(III) ion eight-fold coordinated by two tridentate **L** ligands together with a bidentate nitrate anion (Fig. 4a–e). The Ln(III) ion has a slightly distorted square antiprism for the Ln(III) ion coordination polyhedra (Fig. S5). The coordination of the nitrate anion makes chirality of each complex with equal enantiomers in the crystal lattice (Fig. 4f). The Ln(III) ion coordination numbers, ionic radii, average Ln–O and Ln–N bond lengths for the six complexes are summarized in Table 2. The lack of coordinated methanol in complexes **2**–**6** is due to their smaller ion radii compared to that for Nd(III) ion. Lanthanide contraction has been observed with average bond lengths of Ln–O from 2.468 Å for Nd(III) to 2.299 Å for Lu(III), and Ln–N from 2.614 Å for Nd(III) to 2.442 Å for Lu (III). Unlike complex **1**, complexes **2**–**6** have no obvious intramolecular interactions. However, extensive intermolecular CH-π interactions are present between mononuclear structures in the crystal lattice (Fig. 3b–f). The deprotonated **L** ligand can adopt flexible conformations from fairly flat [7] to twist in complexes **1**–**6** in this work.

2.3. Raman spectroscopy

The vibrational modes of complexes **2**–**5** have been examined using Raman spectroscopy and the Raman band assignments are made with consultation of some relevant literatures [7–10]. The Raman spectra of complexes **2**–**5** (Fig. 5) resemble each other due to the presence of same **L** ligand and similar mononuclear structures. The typical vibrational features related to the **L** ligand include: ν(C=N) + ν(C=C) at ~1565–1562 cm^{-1} and ν(C–C) + ν(CN) at ~1498–1468 cm^{-1} in strong to medium intensity. In addition, Raman bands at 1372, 1065 and 806 cm^{-1} are due to the $(NO_3)^-$ vibrational modes, corresponding to the coordinated $(NO_3)^-$ anion in all complexes **2**–**5**, consistent with their crystal structures. The detailed Raman band assignments are available in Table 4.

2.4. Thermal stability

The thermal stability of complex **2** in air has been investigated. It is thermal stable until ~285 °C where the coordinated **L** ligands start decomposition rapidly with three obvious exotherms at ~325, ~385 and ~430 °C (Fig. 6), respectively, suggesting a complex thermal decomposition process leading to the formation of residue product (Eu_2O_3) after 550 °C, wt% (calc., found): (21.49,

Table 1
Crystal data, structure refinement details and Ln(III) ion coordination environments for complexes **1**–**6**.

Complex	**1**	**2**	**3**	**4**	**5**	**6**
Formula	$C_{46}H_{48}N_7O_7Nd$	$C_{44}H_{40}N_7O_5Eu$	$C_{44}H_{40}N_7O_5Gd$	$C_{44}H_{40}N_7O_5Dy$	$C_{44}H_{40}N_7O_5Ho$	$C_{44}H_{40}N_7O_5Lu$
Formula weight	955.15	898.79	904.08	909.33	911.76	921.80
Crystal system	monoclinic	triclinic	triclinic	triclinic	triclinic	triclinic
Space group	$P2_1/n$	$P\bar{1}$	$P\bar{1}$	$P\bar{1}$	$P\bar{1}$	$P\bar{1}$
a (Å)	18.856(4)	9.3500(19)	9.3400(19)	9.2900(19)	9.2680(19)	9.2500(19)
b (Å)	8.3760(17)	11.060(2)	11.060(2)	11.050(2)	11.138(2)	11.180(2)
c (Å)	27.449(6)	18.380(4)	18.370(4)	18.340(4)	18.191(4)	18.160(4)
α (°)	90	89.58(3)	89.59(3)	89.68(3)	89.96(3)	90.13(3)
β (°)	104.22(3)	87.67(3)	87.82(3)	87.81(3)	87.94(3)	92.31(3)
γ (°)	90	72.53(3)	72.61(3)	72.76(3)	72.76(3)	106.83(3)
V (Å^3)	4202.4(16)	1811.5(7)	1809.6(7)	1796.7(7)	1792.1(7)	1795.9(7)
Z/μ (mm^{-1})	4/1.297	2/1.792	2/1.893	2/2.141	2/2.269	2/2.810
Minimum/Maximum θ [°]	1.187/24.997	1.109/27.907	1.109/27.912	1.111/27.921	1.120/24.998	1.122/24.525
d_{calcd} (g cm^{-3})	1.510	1.648	1.659	1.681	1.690	1.705
Goodness-of-Fit (GOF) on F^2	1.050	1.089	1.101	1.060	1.087	1.008
Final R_1 [a] [$I > 2\sigma(I)$]	0.0336	0.0385	0.0434	0.0266	0.0782	0.0635
Final wR_2 [b] [$I > 2\sigma(I)$]	0.0829	0.0891	0.0994	0.0654	0.2026	0.1417

[a] $R_1 = \Sigma||F_o|-|F_c||/|F_o|$.
[b] $wR_2 = \{\Sigma[w(F_o^2 - F_c^2)^2]/\Sigma[w(F_o^2)^2]\}^{1/2}$.

Table 2
Selected bond lengths (Å) for Ln(III) ion coordination environments of complexes **1**–**6**.

Complex **1**							
Nd1–O1	2.256(2)	Nd1–O2	2.319(2)	Nd1–O3	2.607(3)	Nd1–O4	2.580(2)
Nd1–O6	2.579(2)	Nd1–N1	2.629(3)	Nd1–N2	2.603(3)	Nd1–N4	2.696(3)
Nd1–N5	2.626(3)						
Complex **2**							
Eu1–O1	2.208(3)	Eu1–O2	2.226(3)	Eu1–O3	2.528(3)	Eu1–O4	2.543(3)
Eu1–N1	2.562(3)	Eu1–N2	2.499(3)	Eu1–N4	2.588(3)	Eu1–N5	2.511(3)
Complex **3**							
Gd1–O1	2.199(3)	Gd1–O2	2.222(3)	Gd1–O3	2.530(3)	Gd1–O4	2.520(3)
Gd1–N1	2.544(4)	Gd1–N2	2.481(4)	Gd1–N4	2.569(4)	Gd1–N5	2.496(4)
Complex **4**							
Dy1–O1	2.1777(19)	Dy1–O2	2.1945(18)	Dy1–O3	2.510(2)	Dy1–O4	2.488(2)
Dy1–N1	2.525(3)	Dy1–N2	2.449(2)	Dy1–N4	2.547(2)	Dy1–N5	2.458(2)
Complex **5**							
Ho1–O1	2.177(8)	Ho1–O2	2.189(9)	Ho1–O3	2.512(9)	Ho1–O4	2.465(9)
Ho1–N1	2.497(8)	Ho1–N2	2.447(9)	Ho1–N4	2.503(9)	Ho1–N5	2.437(9)
Complex **6**							
Lu1–O1	2.136(7)	Lu1–O2	2.146(8)	Lu1–O4	2.428(8)	Lu1–O5	2.487(9)
Lu1–N1	2.494(10)	Lu1–N2	2.421(9)	Lu1–N4	2.470(9)	Lu1–N5	2.383(10)

Coordination environment	**1**	**2**	**3**	**4**	**5**	**6**
Ln coordination number	9	8	8	8	8	8
Ln ionic radii (Å)	1.163	1.066	1.053	1.027	1.015	0.977
Mean Ln–O bond (Å)	2.468	2.376	2.368	2.342	2.336	2.299
Mean Ln–N bond (Å)	2.614	2.540	2.523	2.495	2.471	2.442

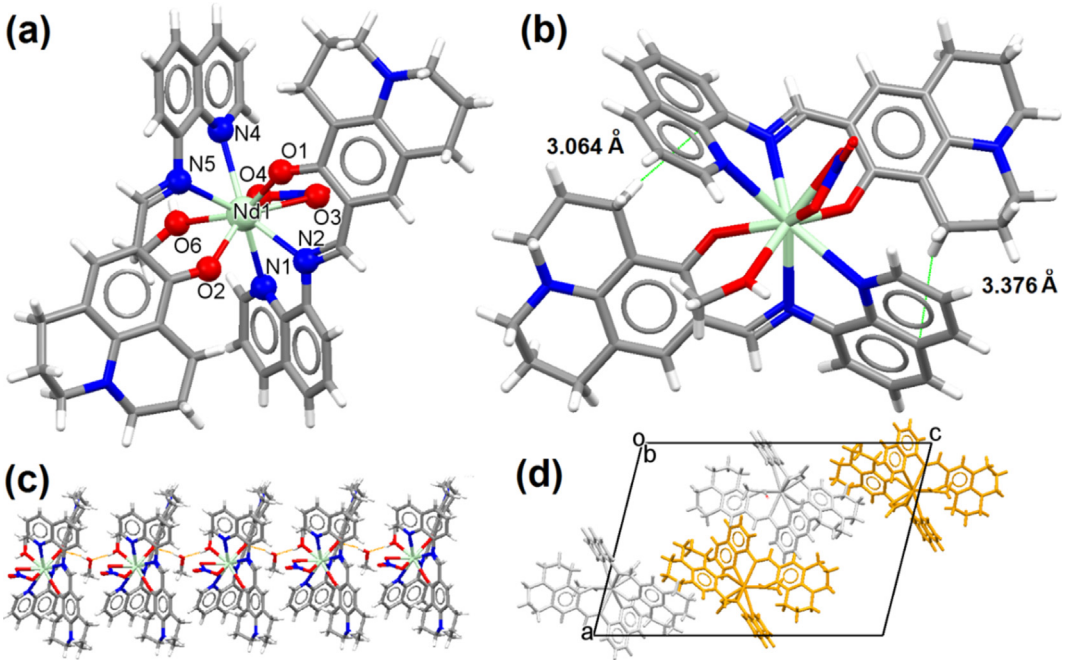

Fig. 2. Mononuclear structure of complex **1** (a), intramolecular CH-π interactions in green lines between the two **L** ligands (b), hydrogen bonded 1D polymer (c) with hydrogen bonds in orange lines and crystal packing along the crystallographic *b*-axis (d) with symmetry generated two enantiomers in different colours in the unit cell.

Table 3
Potential hydrogen bonds calculated with PLATON for complex **1**.

Donor—H···Acceptor	*d*(D—H)	*d*(H···A)	*d*(D···A)	∠(DHA)
O1W—H1W···O2	0.82	2.07	2.83	155
O6—H6···O1W	0.85	1.81	2.65	169

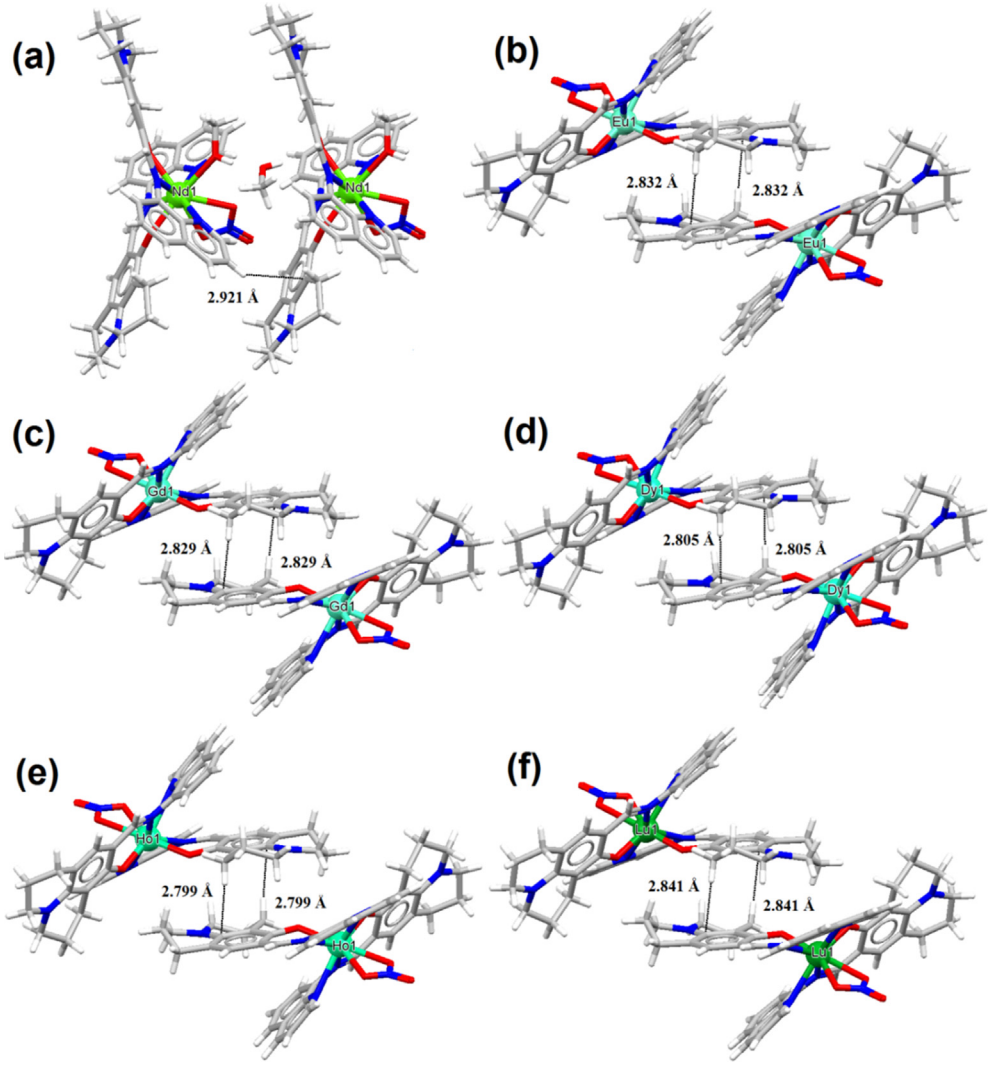

Fig. 3. The intermolecular CH-π interactions in black dotted lines for complexes **1** (a), **2** (b), **3** (c), **4** (d), **5** (e) and **6** (f).

22.38). This is broadly consistent with the thermal stabilities of other Ln complexes with Schiff base ligands [11].

2.5. Magnetic properties

The magnetic properties for complex **3** have been investigated. The results of magnetic property measurements (Fig. 7a) suggest that complex **3** stays paramagnetic in the studied temperature range (2.5–300 K). The analysis of the inverse dc susceptibility with the Curie-Weiss law in the range 200–300 K yields the effective magnetic moment of 7.87(1) μB which is very close to the expected for the free Gd(III) ion (7.94 μB) and the overall magnetic behaviour is typical for lanthanide mononuclear complexes as can be seen from the shape of the $\chi_m T$ product as a function of temperature (Fig. 7a, inset) [12]. The M (μ_B) vs H (magnetic field) data (Fig. 7b) shows consistent results with the magnetic moment per formula unit approaching saturation above ~3 Tesla.

2.6. Electronic structures

The absorption spectra in the ultraviolet and visible region of complexes **1**–**3** measured with solid samples are shown in Fig. 8. Ligand charge transfer (LCT) of **L** contributes to the strong absorption bands in the far UV region, e.g. bands at ~220 nm for complexes **1**–**3** while metal-to-ligand charge–transfer (MLCT) bands at 360 nm and 470 nm for complex **1**; 355 nm, 435 nm and 540 nm for complexes **2** and **3**. In addition, some weak absorption bands in the region of 400–900 nm are present in complex **1,** corresponding to the intraconfiguration transitions of Nd(III) ion. In principle, there are four absorption bands in the visible region typical for a Nd(III) ion located at 520, 585, 745 and 805 nm, corresponding to transitions from the ground state of $^4I_{9/2}$ to the excited states of $^4G_{7/2}$ and $^2K_{13/2}$, $^4G_{5/2}$ and $^2G_{7/2}$, $^4S_{3/2}$ and $^4F_{7/2}$, $^4F_{5/2}$ and $^2H_{9/2}$ [13]. However, only weak absorption bands corresponding to the last three have been observed at 590–565 nm, 760–740 nm and 800 nm, respectively, consistent with the values reported for Nd(III) ions in the literature [14].

3. Conclusions

In the current work, six new lanthanide mononuclear complexes with a julolidine-quinoline based Schiff base ligand have been synthesized by direct complexation reactions in methanol solutions and structurally characterized. In general, mononuclear

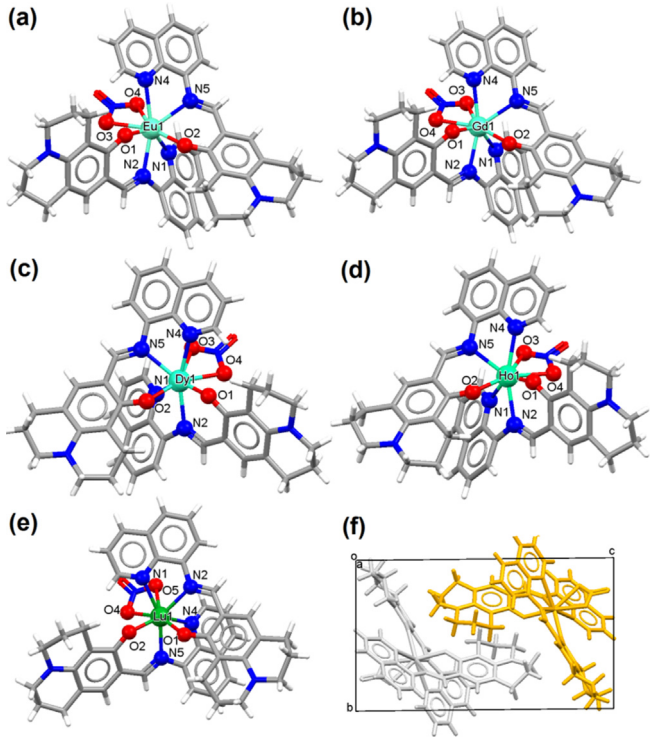

Fig. 4. Crystal structures of complexes **2** (a), **3** (b), **4** (c), **5** (d), **6** (e) and the crystal packing view along the crystallographic *a*-axis (f) with symmetry generated enantiomers in different colours in the unit cell.

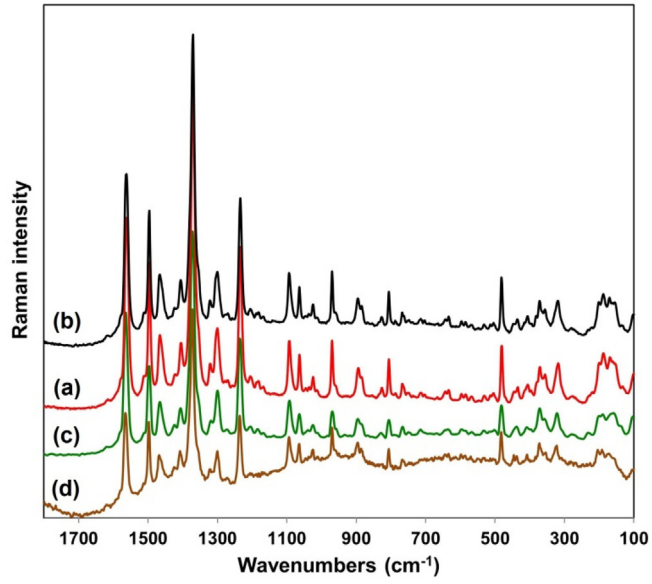

Fig. 5. Raman spectra of complexes **2** (a), **3** (b), **4** (c) and **5** (d) in 1800–100 cm^{-1} region.

structures with Ln to ligand ratio of 1:2 are formed with the Ln(III) ions being nine-fold coordinated by two tridentate ligands and a bidentate nitrate anion except for the complex with Nd(III) ion which is ten-fold coordinated with an additional MeOH molecule due to its relatively larger ionic radius. The coordination of the nitrate anion makes chirality to all complexes with equal enantiomers presence in the solid state. Lanthanide contraction is apparent with the average Ln-O/Ln-N bond lengths decreasing along the lanthanide series. In addition, complex **2** is thermal robust and stable up to 280 °C in air. Other complexes may have similar thermal properties due to the similar mononuclear structures.

4. Experimental

The ligand (H**L**) was synthesized through a 1:1 reaction of 8-hydroxyjulolidine-9-carboxaldehyde and 8-aminoquinoline adapted from a literature method [6]. Other chemicals in A.R. grade were purchased from Sigma-Aldrich and used without further purification. The complexation of H**L** with Nd(III), Eu(III), Gd(III), Dy(III), Ho(III) and Lu(III) ions was carried out using metal nitrates in methanol with metal to ligand ratio of 1:2.

*4.1. Synthesis of [Nd**L**$_2$(NO$_3$)(CH$_3$OH)]·CH$_3$OH (**1**) and [Ln**L**$_2$(NO$_3$)] [Ln = Eu (**2**), Gd (**3**), Dy (**4**), Ho (**5**) and Lu (**6**)]:*

100 mg (0.3 mmol) of H**L** was dissolved in 15 mL of methanol. Lanthanide nitrate hexahydrate [Nd: (65.8 mg, 0.15 mmol); Eu: (66.9 mg, 0.15 mmol); Gd: (67.7 mg, 0.15 mmol); Dy: (68.5 mg, 0.15 mmol); Ho: (68.9 mg, 0.15 mmol); and Lu: (70.4 mg, 0.15 mmol)] in 15 mL of methanol was slowly added to the above ligand solution. Three drops (~0.2 mL) of triethylamine was added under stirring. The mixture was then heated at 60 °C for 30 min. Crystalline products of complexes **1**–**6** were obtained by slow evaporation with 60–80% yields except for complex **6** which had a very low yield allowing only single crystal X-ray diffraction study. Elemental analysis (calculated, found) for complex **1**: C (57.84; 57.75); H (5.07, 5.12); N (10.27, 10.15); complex **2**: C (58.80; 58.77), H (4.49; 4.56), N (10.91; 10.85); complex **3**: C (58.45; 58.41), H (4.46; 4.52), N (10.85; 10.78); complex **4**: C (58.12; 58.08), H (4.43; 4.50), N (10.78; 10.71); complex **5**: C (57.96; 57.88), H (4.42; 4.45), N (10.76; 10.68).

4.2. Characterizations

The elemental analysis was carried out using a Perkin–Elmer 2400 CHN elemental analyser. Scanning electron microscope-energy dispersive spectroscopy (SEM-EDS) was conducted using a Zeiss Ultra Plus SEM (Carl Zeiss NTS GmbH, Oberkochen, Germany) under an accelerating voltage of 15 kV. Powder X-ray diffraction (PXRD) patterns were recorded on a PANalytical X'Pert Pro diffractometer (Almelo, the Netherlands) with Cu Kα radiation (λ = 1.5418 Å) at 45 kV and 40 mA using an angular range of 5–60° two theta in a continuous mode with a step size of 0.02° (2θ) and an acquisition time of 2 s per step. Raman spectra were recorded on a Renishaw inVia spectrometer equipped with a 514 nm excitation Ar laser in the range of 2000–100 cm^{-1} with a spectral resolution of ~1.7 cm^{-1}. UV–Vis absorption spectra were collected on an Agilent Cary 5000 spectrophotometer equipped with a Labsphere Biconical Accessory. Spectra were referenced to that of a Labsphere certified standard (Spectralon), and transformed into Kubelka-Munk units, $F(R) = (1-R)^2/2R$ [15]. Thermogravimetric and differential thermal analysis (TG/DTA) were performed in air with a heating rate of 5 °C/min using a Netzsch STA 449F3 Jupiter (Germany) apparatus with a normal gas flow-rate of 50 mL/min. An alumina crucible was used for the experiment and aluminum oxide was used as the reference material. Magnetic susceptibility data for complex **3** were collected using a PPMS9 magnetometer (Quantum Design) calibrated against a standard palladium sample. Zero-field cooled DC susceptibility was measured under the field of 1000 Oe

Table 4
Raman bands and assignments for complexes **2**–**5**.

Raman band position (cm^{-1})				Raman assignment
Complex **2**	Complex **3**	Complex **4**	Complex **5**	
1562 s	1563 s	1564 s	1565 s	ν (C=C) + ν (C=N) (ring stretch vibration)
1496 s	1497 s	1497 s	1498 s	ν (CC) + ν (CN)
1465 m	1466 m	1466 m	1468 m	ν (CC) + ν (CN)
1405 m-w	1406 m-w, sh	1406 m-w, sh	1408 m-w, sh	ring stretch vibration
1370 vs	1371 vs	1372 vs	1372 vs	ν (NO_3), (ν_3 antisymmetric stretching vibration); δ (CH)
1321 w, 1300 m	1320 w, 1300 m	1320 w, 1300 m	1320 w, 1300 m	ν (C–N) + δ (CH), in-plane bending; τ (CH_2)
1234 s	1234 s	1235 s	1235 s	δ (CH), ring C–H deformation vibration
1182 vw	–	1184 vw	–	δ (CH), in-plane bending + ν (CO)
1093 m	1093 m	1093 m	1094 m	δ (CH), in-plane bending + δ (CNC), ν (CC)
1064 m	1064 m	1064 m	1065 m-w	ν (NO_3), (ν_1 symmetric stretching vibration)
1024 w	1025 w	1025 w	1025 w	Ring vibration
970 m	970 m	970 m	970 m	Ring vibration
894 m, br	895 w-m, br	895 w-m, br	896 w-m, br	δ (CH), out-of-plane bending + δ (CCC) + δ (CCN)
806 m	806 m	806 m	806 m	δ (ONO) in NO3
767 w	767 vw	767 vw	767 vw	δ (ONO)
634 w	633 vw	636 vw	–	In plane ring deformation
481 m	481 m	481 m	481 m	Out of plane ring deformation; δ (ONO) bending mode
435 w	–	438 vw	446 vw	δ (C–O); δ (CNC) + δ (CCN)
406 w	406 vw	408 vw	408 vw	δ (CCN)
370–356 w-m, br	372–355 w-m, br	371–355 w-m, br	372–355 w-m, br	ν (M–N) + ν (M–O), stretching vibrations
318 m	319 m	322 m-w	323 m-w	τ (C–N), ring C–H deformation vibration
188–170 m, br	188–170 m, br	190–159 m, br	192 w, br	Lattice modes

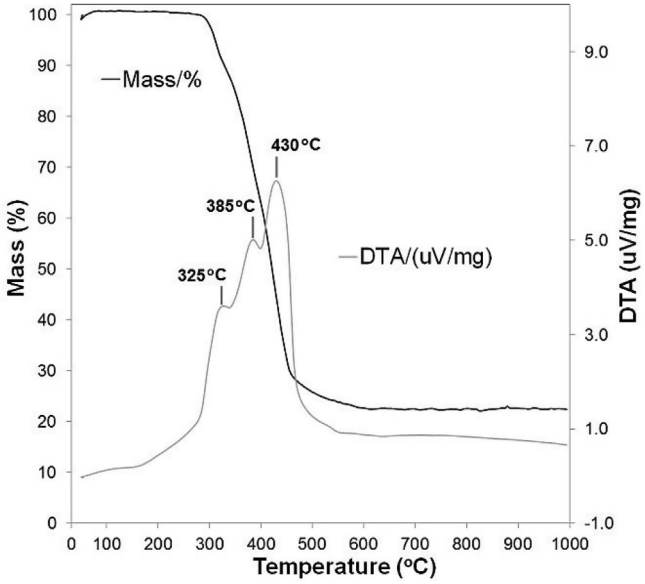

Fig. 6. Thermogravimetric and differential thermal analysis results for complex **2**.

in the range 2–300 K. The data were corrected for diamagnetism using the Pascal's constants.

4.3. Single crystal X-ray diffraction

The single crystal X-ray diffraction measurements for complexes **1**–**6** were carried out on the MX1 beamline [16] at the Australian Synchrotron. Diffraction data were collected using Si<111> monochromated synchrotron X-ray radiation (λ = 0.71074) at 100 (2) K with BluIce software [17] and were corrected for Lorentz and polarization effects using the XDS software [18]. An empirical absorption correction was then applied using SADABS [19]. The structures were solved by direct methods and the full-matrix least-squares refinements were carried out using a suite of SHELXL program [20] via Olex^2 interface [21]. All non-hydrogen atoms were located from the electron density maps and refined anisotropically.

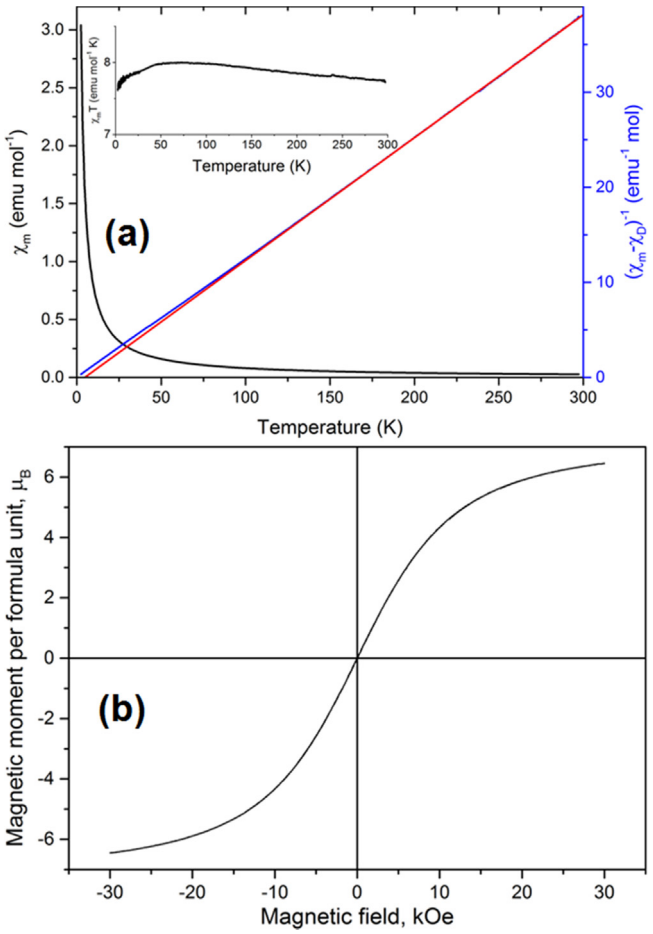

Fig. 7. Magnetic results for complex **3**: (a) χ_m and (χ_m-χ_D) vs. T with an inset of $\chi_m T$ vs. T, and (b) M vs. H data.

Hydrogen atoms were added in the ideal positions and refined using a riding model. Potential hydrogen bonds were calculated using PLATON [22].

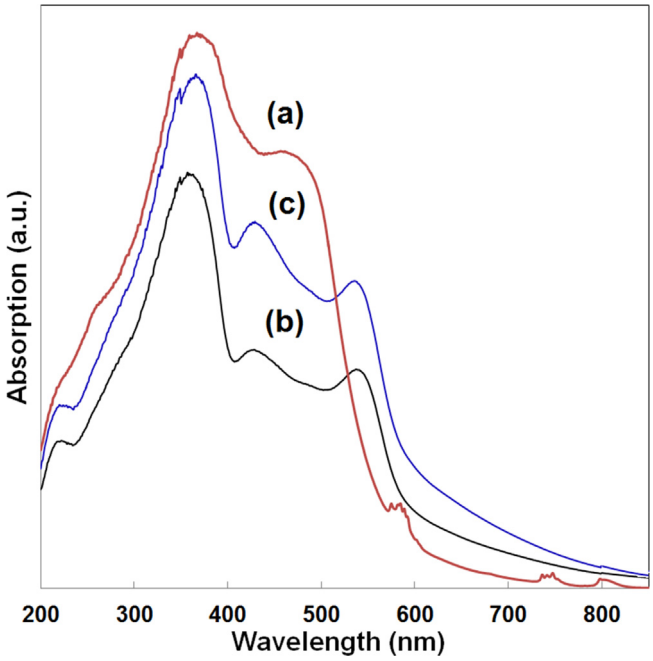

Fig. 8. UV–Vis absorption spectra for complexes **1** (a), **2** (b) and **3** (c).

Acknowledgements

The authors would like to thank Dr. F. Li for helpful discussion. The crystallographic data collections for complexes **1–6** were undertaken on the MX1 beamline at the Australian Synchrotron, a part of ANSTO.

Appendix A. Supplementary data

CCDC 1892111–1892116 contain the supplementary crystallographic data for complexes **1–6**. These data can be obtained free of charge via http://www.ccdc.cam.ac.uk/conts/retrieving.html, or from the Cambridge Crystallographic Data Centre, 12 Union Road, Cambridge CB2 1EZ, UK; fax: (+44) 1223-336-033; or e-mail: deposit@ccdc.cam.ac.uk. Supplementary data to this article can be found online at https://doi.org/10.1016/j.poly.2019.03.017.

References

[1] (a) P.A.S. Smith, T.Y. Yu, J. Org. Chem. 17 (1952) 1281;
(b) J.M. Kauffman, S.J. Imbesi, M.A. Aziz, Org. Prep. Proced. Int. 33 (2001) 603;
(c) J.J. Holt, B.D. Calitree, J. Vincek, M.K. Gannon, M.R. Detty, J. Org. Chem. 72 (2007) 2690.
[2] (a) D. Maity, A.K. Manna, D. Karthigeyan, T.K. Kundu, S.K. Pati, T. Govindaraju, Chem. Eur. J. 17 (2011) 11152;
(b) Y.J. Na, I.H. Hwang, H.Y. Jo, S.A. Lee, G.J. Park, C. Kim, Inorg. Chem. Commun. 35 (2013) 342;
(c) K.B. Kim, G.J. Park, H. Kim, E.J. Song, J.M. Bae, C. Kim, Inorg. Chem. Commun. 46 (2014) 237;
(d) J. Jun Lee, G. Jin Park, Y. Sung Kim, S. Young Lee, H. Ji Lee, I. Noh, C. Kim, Biosens. Bioelectron. 69 (2015) 226.
[3] (a) J.H. Lee, S.H. Lee, Y.A. So, G.J. Park, C. Kim, B. Korean Chem. Soc. 36 (2015) 1618;
(b) T.G. Jo, Y.J. Na, J.J. Lee, M.M. Lee, S.Y. Lee, C. Kim, New J. Chem. 39 (2015) 2580;
(c) T.G. Jo, Y.J. Na, J.J. Lee, M.M. Lee, S.Y. Lee, C. Kim, Sensor. Actuat. B-Chem. 211 (2015) 498.
[4] (a) G.J. Park, I.H. Hwang, E.J. Song, H. Kim, C. Kim, Tetrahedron 70 (2014) 2822;
(b) S.A. Lee, G.R. You, Y.W. Choi, H.Y. Jo, A.R. Kim, I. Noh, S.-J. Kim, Y. Kim, C. Kim, Dalton Trans. 43 (2014) 6650;
(c) Y.S. Kim, G.J. Park, J.J. Lee, S.Y. Lee, S.Y. Lee, C. Kim, RSC Adv. 5 (2015) 11229.
[5] J.Y. Noh, S. Kim, I.H. Hwang, G.Y. Lee, J. Kang, S.H. Kim, J. Min, S. Park, C. Kim, J. Kim, Dyes Pigments 99 (2013) 1016.
[6] G.J. Park, Y.J. Na, H.Y. Jo, S.A. Lee, C. Kim, Dalton Trans. 43 (2014) 6618.
[7] D.J. Fanna, Y. Zhang, L. Li, I. Karatchevtseva, N.D. Shepherd, A. Azim, J.R. Price, J. Aldrich-Wright, J.K. Reynolds, F. Li, Inorg. Chem. Front. 3 (2016) 286.
[8] Y. Zhang, D.J. Fanna, N.D. Shepherd, I. Karatchevtseva, K. Lu, L. Kong, J.R. Price, RSC Adv. 6 (2016) 75045.
[9] D.J. Fanna, Y. Zhang, A. Salih, J.K. Reynolds, F. Li, J. Coord. Chem. 69 (11–13) (1883) (2016).
[10] (a) G. Socrates, Infrared and Raman Characteristic Group Frequencies: Tables and Charts, 3rd ed., John Wiley & Sons Hoboken, New York, 2004;
(b) R.L. Frost, Anal. Chim. Acta 517 (2004) 207;
(c) C.A. Tellez, S.E. Hollauer, M.A. Mondragon, V.M. Castano, Spectrochem. Acta A 57 (2001) 993;
(d) S.A. Brandan, F.M. Lopez, M. Montejo, J.J. Lopez Gonzales, A.B. Altabef, Spectrochem. Acta A 75 (2010) 1422.
[11] (a) H.-M. Guo, Asian J. Chem. 21 (2009) 1113;
(b) Z.A. Taha, A.M. Ajlouni, J. Al-Mustafa, Chem. Pap. 67 (2013) 194.
[12] J.-P. Costes, F. Dahan, A. Dupuis, S. Lagrave, J.-P. Laurent, Inorg. Chem. 37 (1998) 153.
[13] S. Sun, H. Zhang, H. Yu, H. Xu, J. Wang, J. Mater. Res. (2012) 2528.
[14] T. Jensen, V.G. Ostroumov, J.P. Meyn, G. Huber, A.I. Zagumennyi, L.A. Shcherbalov, Appl. Phys. B 58 (1994) 373.
[15] W.W. Wendlandt, H.G. Hecht, Reflectance Spectroscopy, Wiley Interscience, New York, 1966.
[16] D. Aragao, J. Aishima, H. Cherukuvada, R. Clarken, M. Clift, N.P. Cowieson, D.J. Ericsson, C.L. Gee, S. Macedo, N. Mudie, S. Panjikar, J.R. Price, A. Riboldi-Tunnicliffe, R. Rostan, R. Williamson, T.T. Caradoc-Davies, J. Synchrotron Rad. 25 (2018) 885.
[17] T.M. McPhillips, S.E. McPhillips, H.J. Chiu, A.E. Cohen, A.M. Deacon, P.J. Ellis, E. Garman, A. Gonzalez, N.K. Sauter, R.P. Phizackerley, S.M. Soltis, P. Kuhn, J. Synchrotron Rad. 9 (2002) 401.
[18] W. Kabsch, Acta Cryst. D66 (2010).
[19] SADABS: Empirical Absorption and Correction Software, University of Göttingen, 1996.
[20] G.M. Sheldrick, Acta Cryst. C. 71 (2015) 3.
[21] O.V. Dolomanov, L.J. Bourhis, R.J. Gildea, J.A.K. Howard, H. Puschmann, J. Appl. Cryst. 42 (2009) 339.
[22] A.L. Spek, Acta Cryst. Section D D65 (2009) 148.